Int J Adv Manuf Technol (2015) 77:621–628
DOI 10.1007/s00170-014-6474-3

ORIGINAL ARTICLE

Weld bead formation and corrosion behavior of pulsed laser welded zirconium alloy

Chuang Cai · Wang Tao · Liqun Li · Yanbin Chen

Received: 3 December 2013 / Accepted: 7 October 2014 / Published online: 21 October 2014

Abstract Pulsed laser spot welding was developed for the fabrication of Zircaloy spacer grid assembly in pressurized light water reactors. The effects of laser welding parameters on the size of the weld beads were discussed. The influence of oxygen and hydrogen uptakes during the welding process on the corrosion resistance was investigated after the corrosion tests. The results indicate that the optimum weld bead size could be obtained by adjusting the pulsed laser parameters, including laser peak power, number of shots, and pulse width. Pulse width should be taken into consideration to control the weld width. When the moisture and oxygen contents were maintained at a low level, i.e., 200 parts per million (ppm) and 30 ppm, respectively, the oxide thickness of specimens corroded for 120 h was about 0.7 μm compared to about 1.5 μm at high moisture and oxygen contents (1,000 and 280 ppm). The combination of the oxidation and hydriding induced cracking was responsible for the crack of the specimens welded under high moisture and oxygen contents, thereby decreasing the corrosion resistance of the welding specimens.

Keywords Spacer grid assembly · Pulsed laser spot welding · Weld bead size · Moisture and oxygen contents · Corrosion resistance

1 Introduction

The Zircaloy spacer grid assembly is one of the major structural components in pressurized light water reactors to support and maintain the fuel rods laterally and vertically [1–4]. The control of the weld bead size is of vital importance, since the spacer grid assembly is fabricated by welding the intersected straps at the intersection points. From the structural point of view, the weld beads of spacer grid assembly are required to be immune to wear the fuel rods. Besides, flow channels are provided by the spacer grid assembly between the fuel rods, which assist the heat radiation from the fuel pellets to the coolant in the reactor [5]. The size of weld beads should be small enough to decrease the pressure drop level of the coolant.

The corrosion is one of the main factors in the degradation of the spacer grid assembly during service, since the operating condition of the spacer grid assembly is high temperature and high pressure. The reaction between the Zircaloy and the coolant in the reactor leads to the oxidation and the hydrogen uptake. It was observed from the reports that the authors are concentrating on the corrosion mechanism of Zircaloy [6–11]; therefore, many questions concerning the corrosion of Zircaloy welded specimens still remain open. At elevated temperature, zirconium and its alloy have a high absorption of oxygen and hydrogen in the atmosphere because of the chemistry activity. During the welding process, the oxygen and hydrogen uptakes would take place in the weld bead if the moisture and oxygen contents in the chamber exceed the limits. Consequently, the corrosion resistance of the weld bead is closely related to the oxygen and hydrogen uptakes mentioned above.

In this paper, the formation of the weld bead from the intersection point was examined. The effects of laser welding parameters on the weld beads size of spacer grid assembly were discussed. The welding of the intersection points were performed in the chamber of different moisture and oxygen contents. The influence of oxygen and hydrogen uptakes on the corrosion resistance was studied after the corrosion tests in the autoclave.

C. Cai · W. Tao · L. Li (✉) · Y. Chen
State Key Laboratory of Advanced Welding and Joining,
Harbin Institute of Technology, Harbin 150001, China
e-mail: liliqun@hit.edu.cn

Table 1 The chemical composition of Zircaloy straps (in mass fraction %)

	Nb	Sn	Fe	Zr
Zircaloy	1.0	1.0	0.1	Bal.

2 Experimental procedure

2.1 Alloy materials

In the present work, 0.457-mm-thick Zircaloy (Zr-Nb-Sn-Fe) grid straps were used. The chemical composition of this material is presented in Table 1. The straps were thinned to 0.457 mm by a series of hot and cold rolling during the manufacturing process. In accordance with the assembly requirements, the straps with grooves and protruding intersections were fabricated, as shown in Fig. 1. Before pulsed laser spot welding process, the straps were cleaned using acetone for about 30 min by ultrasonic wave cleaner.

2.2 Spacer gird assembly

A spacer grid assembly is an interconnected array of grid straps fabricated by welding the straps at intersection points, as shown in Fig. 1. For pressurized light water reactor, Inconel and Zircaloy spacer grid assemblies are prevailing in fuel assembly. The former is made of Inconel straps because of its high corrosion resistance and strength. And, the Inconel spacer grid assembly could be fabricated by brazing. The latter is made of Zircaloy straps for its low thermal neutron absorption cross section, high strength, and good corrosion resistance even at elevated temperature. The Zircaloy spacer grid assembly could be welded by tungsten inert gas (TIG) welding, laser beam welding (LBW), and electron beam welding (EBW). Currently, LBW is the main method for the manufacturing of Zircaloy spacer grid assembly in the interest of small weld beads and larger penetration depth [2]. Compared with continuous wave mode lasers, pulsed lasers transfer a minimum amount of energy to workpieces with high

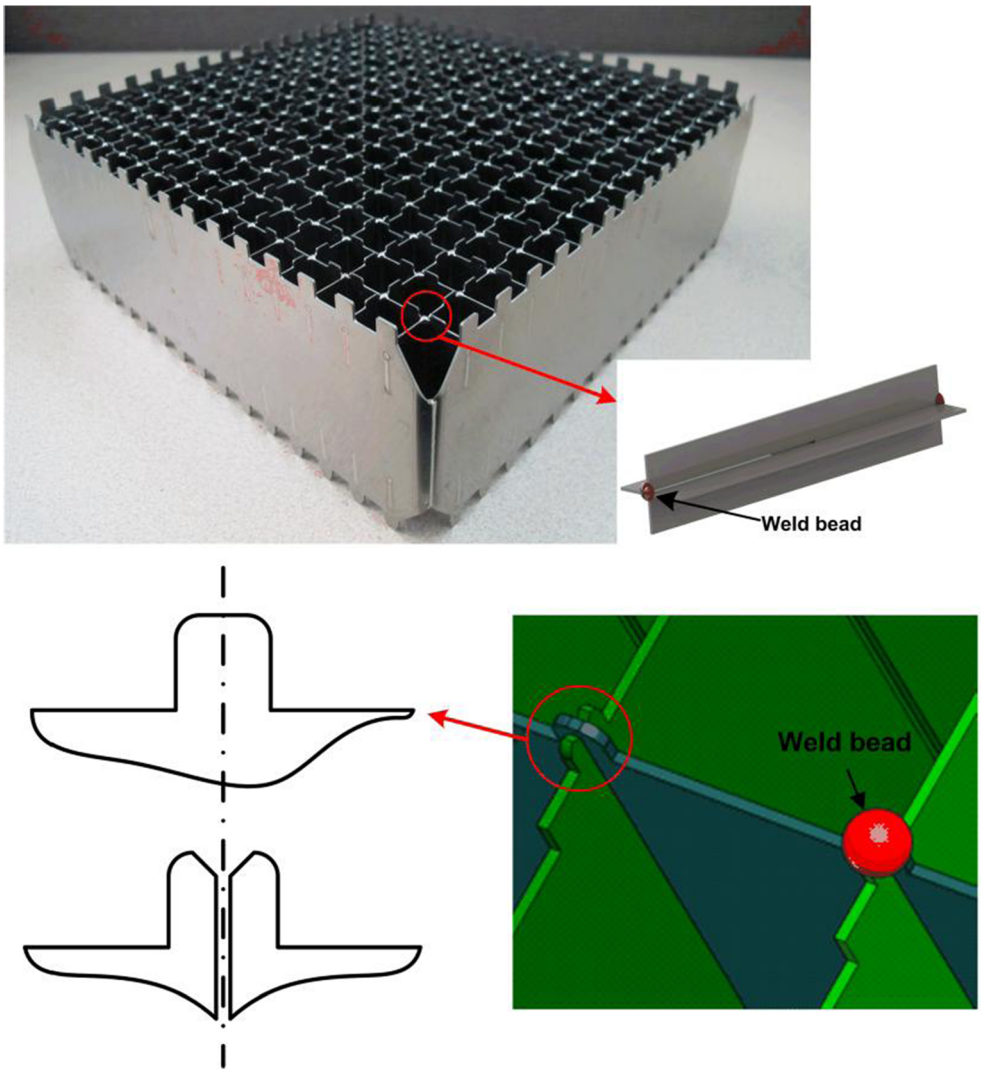

Fig. 1 Schematic diagram of the spacer grid assembly

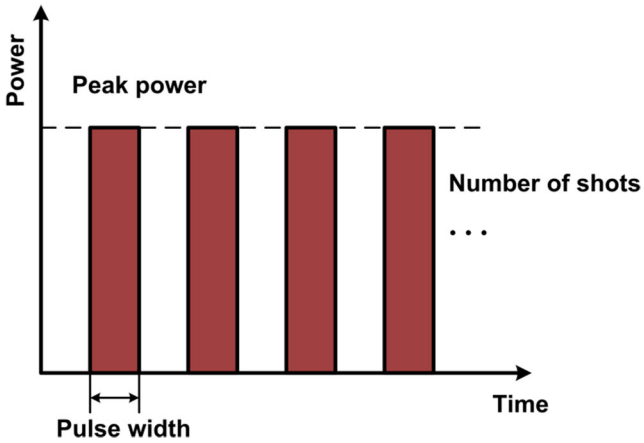

Fig. 2 Schematic diagram of pulsed laser

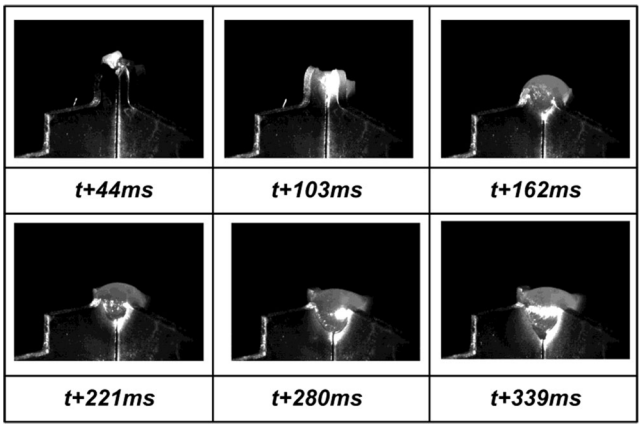

Fig. 3 The formation of the weld bead

precision [12–16], which is particularly suited to the welding of intersection points of spacer grid assembly.

2.3 Pulsed laser spot welding

A set of fully automatic equipment has been developed for the welding of spacer grid assembly which integrates the laser unit, control system, and double chambers. A pulsed Nd:YAG laser (TRUMPF TruPulse 556) with a maximum peak power of 10 kW was used. The pulsed Nd:YAG laser with wavelength of 1,064 nm was delivered to processing head through an optical fiber of 600-μm diameter. The diameter of the beam spot was 0.9 mm. The laser beam was irradiated through the quartz glass on the top of the chamber. The pulsed laser spot welding process was conducted in a chamber which was equipped with positioner for the all position welding. Coaxial charge-coupled device (CCD) was used for points centering and real-time monitoring during the welding process. The moisture and oxygen contents in the chamber were monitored using corresponding analyzers. Pure argon (99.999 %) with a continuous flow rate of 60 L/min was provided to the chamber after its vacuum degree was below 40 mbar to control the moisture and oxygen contents and improve the heat radiation in the chamber. Numerical control system was adopted to facilitate automatization during the manufacture of the spacer grid assembly. A high-speed video (CamRecord 5000-2) with the frame rate of 5,000 frames per second and semiconductor laser source (Cavilux HF) were positioned to monitor the forming process of weld beads.

In order to obtain a minimum amount of energy to the intersection points with high precision, pulsed laser in rectangular mode was conducted, as shown in Fig. 2. The pulsed laser parameters including laser peak power, pulse width, and number of shots are shown in the schematic diagram. Table 2 shows the specifications of a pulsed Nd:YAG laser used in this study, and the laser pulse frequency was kept constant at 17 Hz during the whole process.

Table 2 Specifications of pulsed Nd:YAG laser

Welding parameters	Value
Laser peak power P_p (W)	2,600–3,100
Pulse width t (ms)	8–10
Number of shots n	4–7
Laser pulse frequency f (Hz)	17

2.4 Corrosion tests

The corrosion samples were cut from the space grid assembly at the midpoint of two adjacent intersection joints, as illustrated in Fig. 1. Before the corrosion tests, the samples were cleaned using acetone for about 30 min by ultrasonic wave cleaner. Corrosion tests were performed in 400 °C steam under the pressure of 10.3 MPa. The tests were operated in a standard consistent with the ASTM practice for Aqueous Corrosion Testing of Samples of Zirconium and Zirconium Alloys (G2-88). The samples were corrosion-tested in autoclave for 120 h. The corrosion behavior was evaluated by examining the amount of hydrides and measuring the oxide thickness as a function of exposure time after the corrosion tests.

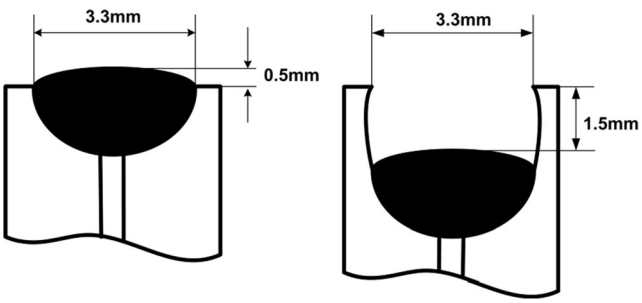

Fig. 4 The limits of weld bead size

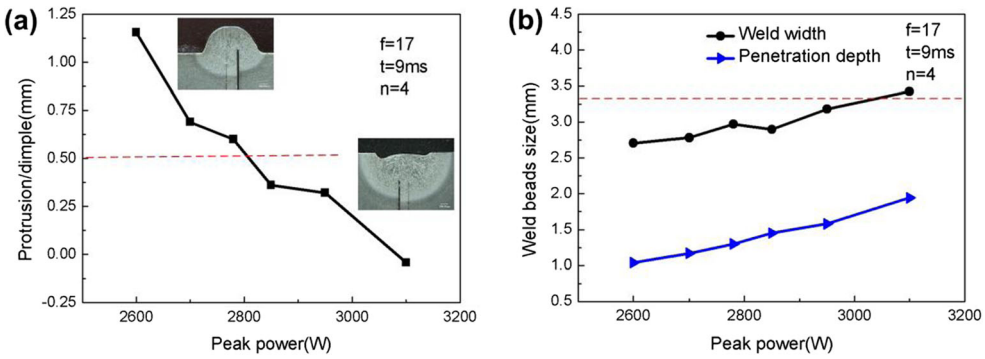

Fig. 5 Weld bead size as a function of laser peak power. **a** Protrusion or dimple and **b** weld width and penetration depth

2.5 Sample preparation

The standard metallographic preparation procedures were utilized to examine the macrography of weld beads, and the morphology and distribution of hydrides. Cross-sectional specimens were grinded, polished, and etched in a solution of 5 vol% HF+45 vol% HNO_3+50 vol% H_2O for about 3 min, and then rinsed in cold tap water and alcohol. The VHX-1000 metallurgical optical microscopy was employed for the microstructure examination. The weld beads were measured by the measure tool of the metallurgical microscopy with an accuracy of 0.1 μm. After the corrosion tests, the cross sections of the oxides were observed by using S-3400 N scanning electron microscopy.

3 Results and discussion

3.1 Weld bead formation

Figure 3 illustrates the formation of the weld bead during the pulsed laser spot welding process. The weld bead was preformed after the first three laser pulses were irradiated the intersection point one by one. The protruding intersection melted at the initial stage of the pulsed laser welding process, thereby producing sufficient molten metal. The molten metal maintained by the laser-induced energy flowed along the intersection line under the gravity and surface tension, and then produced the intersection joint of the straps.

The function of the spacer grid assembly is to maintain and support the fuel rods in the reactor. The spacer grid assembly with unqualified weld bead size gives rise to the wear of fuel rods and a large pressure drop of the coolant. Figure 4 indicates that the weld width of the weld beads should be no more than 3.3 mm. Moreover, the protrusion or dimple of the weld beads should be between the convex and depress limits, i.e., 0.5 and 1.5 mm, respectively.

Generally, it is known from the literature that if the value of the power density is more than 10^6 W/cm^2, the laser welding could be characterized as keyhole welding [17]. In this experiment, the power density values which could be calculated as per the following equation were varying from 4.08×10^5 to 4.87×10^5 W/cm^2. Consequently, it could be expected that the mode of pulsed laser spot welding would be conduction phenomena rather than keyhole phenomena.

$$\text{Power density} = \text{Laser peak power}\left(P_p\right)/\text{Beam spot area}$$

The weld bead sizes were determined by the energy transferred to the intersection points. In this experiment,

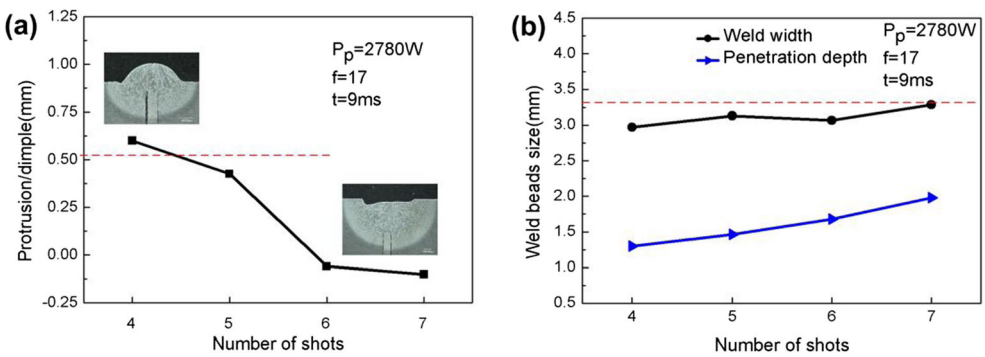

Fig. 6 Weld beads size as a function of number of shots. **a** Protrusion or dimple and **b** weld width and penetration depth

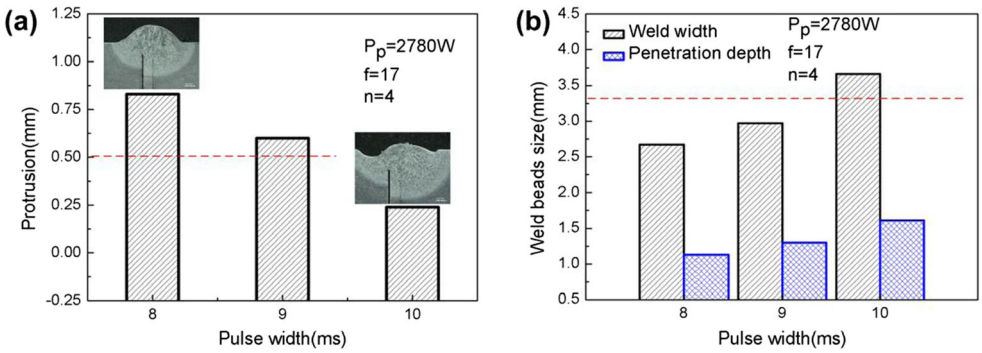

Fig. 7 Weld beads size as a function of pulse width. **a** Protrusion and **b** weld width and penetration depth

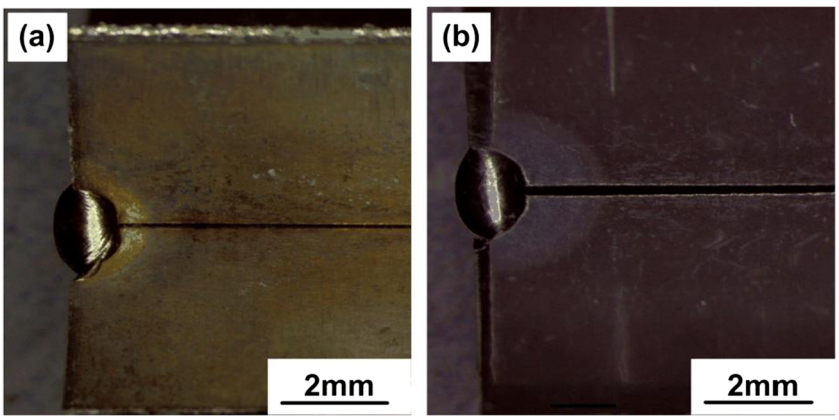

Fig. 8 Optical macrographs of weld bead. **a** As-welded and **b** corroded

the energy obtained by the intersection points was related to the parameters, including laser peak power, pulse width, and number of shots when the laser pulse frequency remained unchanged:

$$\text{Energy per pulse} = \text{Laser peak power}\left(P_p\right) \times \text{Pulse width}(t)$$

$$\text{Total energy} = \text{Energy per pulse} \times \text{Number of shots}(n)$$

Obviously, the weld beads size including weld penetration depth and weld width increased as the welding parameters increase.

Figure 5a, b shows that laser peak power ranging from 2,800 to 3,100 W was sufficient to produce the weld beads with required protrusion and weld width, with the pulse width and number of shots kept as constant, i.e., 9 ms and 4, respectively. As for the number of shots, the optimum parameter was ranging from 5 to 7 to meet the weld bead size standard, as shown in Fig. 6a, b. Figure 7a, b illustrates that the weld beads with protrusion below 0.5 mm could be obtained when pulse width was more than 9 ms; however, the weld beads with excess weld width made the spacer grid assembly unqualified. From the ensemble observations, the qualified weld beads could be derived by decreasing the pulse width and increasing the laser peak power or number of shots properly.

3.2 Corrosion behavior of weld beads

Figure 8 illustrates the appearances of intersected weld bead before and after the corrosion tests. Compared with the sample in the as-welded condition (Fig. 8a), black oxides were observed on the sample after the corrosion tests, as shown in Fig. 8b. Hydrogen and oxygen uptakes occurred during the corrosion tests of the weld beads. Consequently, the zirconium was present as ZrO_2 on the surface of the samples. The hydrogen was present as zirconium hydrides in the interior of the weld beads. During the corrosion tests process, the H^+ ions was ionized from the corrosion medium. Hydrogen atoms were formed as the electrons on the surface of the oxides were captured by the H^+ ions. Some of the hydrogen atoms diffused into the metal through the oxide/metal interface. Moreover, the second-phase particles embedded in the metal matrix and exposed at the metal/oxide interface could act as a preferred path for hydrogen uptake [18]. Generally, it was found in the literature that the limited solid solubility of hydrogen in

Table 3 The moisture and oxygen contents of the chamber (parts per million ppm)

	Moisture	Oxygen
#1	1,000	280
#2	200	30

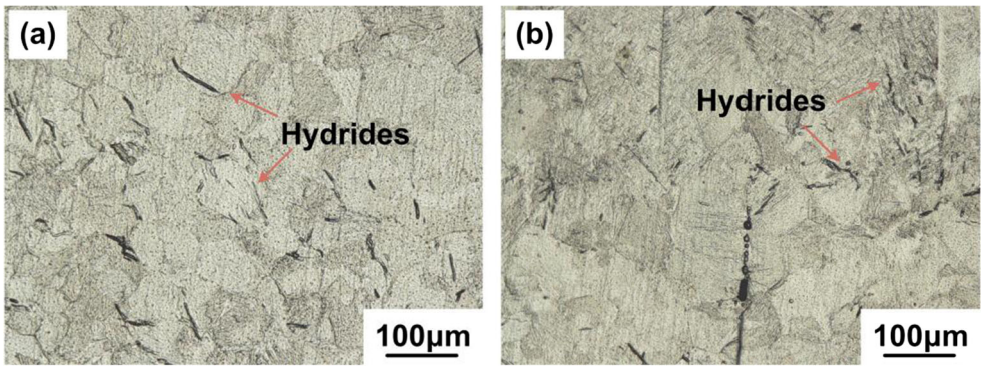

Fig. 9 Optical micrographs of hydrides after corrosion tests **a** #1 and **b** #2

zirconium alloys was low at the temperatures of 400 and 25 °C, i.e., 200 and 1 μg/g [19]. The hydride precipitation occurred when the hydrogen contents exceeded the limited solid solubility.

During the pulsed laser spot welding process, the moisture and oxygen contents of the chamber exerted significant influence on the corrosion resistance of the weld beads. In this experiment, two kinds of welding conditions, as shown in Table 3, were provided to discuss the effects of moisture and oxygen contents on the corrosion resistance.

Figure 9 shows the microstructure of the weld beads among which the black elongated hydrides were distributed. The amount of the hydrides in specimens welded under condition #1 was noticeably larger than that under condition #2. During the pulsed laser spot welding process, the big thermal gradient was generated along the radical direction of the points when the laser acted on the intersection points perpendicularly. When the welding was performed under condition #1, the hydrogen ingress was higher during the melting and cooling processes of the intersection points than that under condition

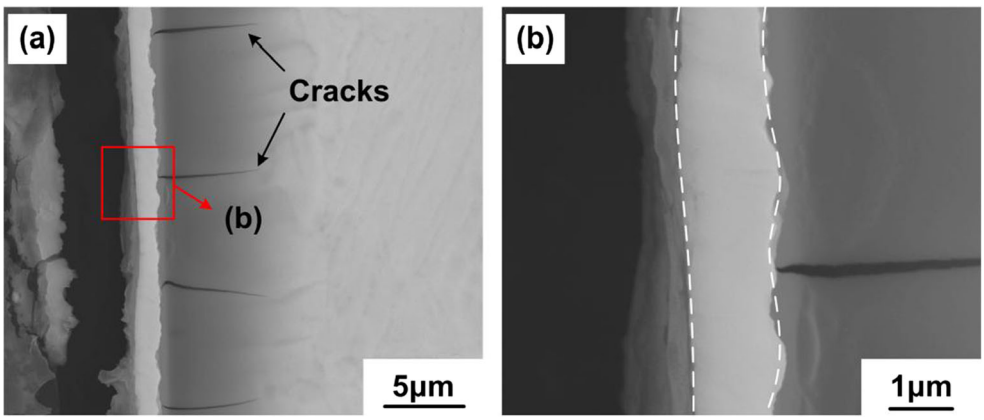

Fig. 10 Electron micrographs of the oxides formed on the specimen welded under condition #1. **a** Low magnification and **b** high magnification

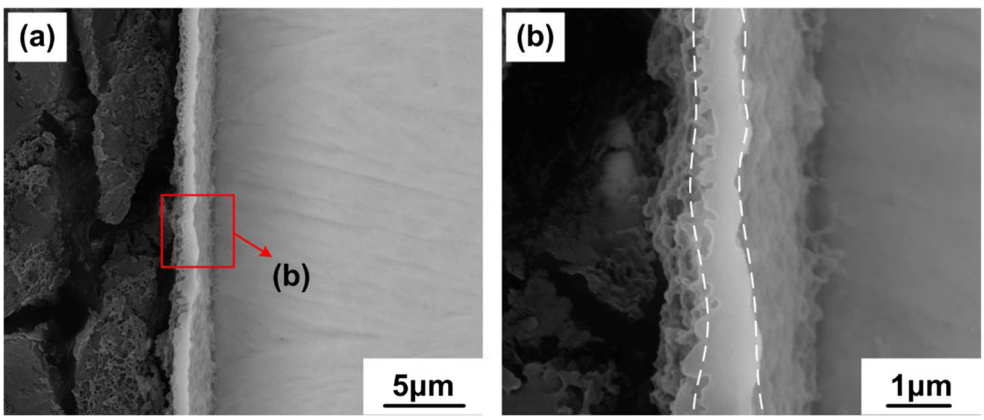

Fig. 11 Electron micrographs of the oxides formed on the specimen welded under condition #2. **a** Low magnification and **b** high magnification

#2. Thereby, after the corrosion tests, the hydride precipitation in the samples increased with the increasing moisture and oxygen contents in the chamber during the welding process.

Accompanied with the hydrogen uptake, the oxides were formed on the surface of the weld beads. The areas indicated by the dotted lines were the oxides, as shown in Figs. 10 and 11, respectively. It could be observed that the thickness of oxide film formed on the specimens welded under condition #1 was noticeably higher than that under condition #2, i.e., about 1.5 and 0.7 μm, respectively. Moreover, the cracks basically initiated from the oxide/metal interface and then propagated into the metal perpendicularly were observed in specimens welded under condition #1 after the corrosion tests, as shown in Fig. 10.

The different corrosion resistance of the intersected weld beads were ascribed to the stress at the oxide/metal interface. The formation of ZrO_2 film on the weld beads was accompanied with the volume dilatation, thereby resulting in a constraint in the surrounding of the yet-to-be-oxidized metal. In addition, the high Pilling-Bedworth ratio (about 1.56 [20]) of ZrO_2/Zr led to the buildup of macroscopic compressive stress in the oxide film during the corrosion process. Since the pre-oxides formed due to the high moisture and oxygen contents during the welding process, the compressive stress of oxide film was very intense. It was well known that the oxidation of weld beads takes place at the oxide/metal interface. The oxide film was subjected to a stress gradient rising from the outer surface to the oxide/metal interface which gave rise to the tensile stress in the metal. The microstructural defects (e.g., vacancies and dislocations) produced by the existence of the stress gave rise to the trapping effect for hydrogen diffusion [21]. The diffusion of hydrides exerted a closely influence on the overall hydride precipitation rate [22]. Besides, the microstructural defects provided the preferred nucleation sites for hydrides [23]. The gathered microstructural defects prompted the generation of micro-cracks in the metal under the stress. The hydride precipitation induced by the tensile stress field in the metal occurred at the micro-crack tips. The enrichment of the brittle hydrides resulted in the propagation of the cracks. Consequently, the oxidation of the yet-to-be-oxided metal was aggravated as a result of the increasing contact area of the corrosion medium and metal. This will in return induce the stress in the metal. From the ensemble observations, the combination of the oxidation and hydriding induced cracking was responsible for the crack of the specimens welded in the chamber with high moisture and oxygen contents after the corrosion tests.

4 Conclusions

(1) Pulsed laser spot welding has been employed in welding of the intersection points of spacer grid assembly. The optimum weld bead size could be obtained by adjusting the pulsed laser parameters, including laser peak power, number of shots, and pulse width. Pulse width should be taken into consideration to control the weld width.

(2) The moisture and oxygen contents of the chamber during the pulsed laser spot welding process exerted significant influence on the corrosion resistance of the weld beads. When the moisture and oxygen contents were maintained at a low level, i.e., 200 and 30 ppm, respectively, the oxide thickness of specimens corroded for 120 h was about 0.7 μm compared to 1.5 μm of high moisture and oxygen contents (1,000 and 280 ppm).

(3) The combination of the oxidation and hydriding induced cracking is responsible for the crack of the specimens welded under high moisture and oxygen contents, thereby decreasing the corrosion resistance of the welding specimens.

Acknowledgments The authors would like to thank Liang Qiao for his assistance in the pulsed laser spot welding experiments. We also express our gratitude to Huirong Zhao and Xue Hou for the assistance in corrosion tests. Dr. Caiwang Tan is gratefully acknowledged for his valuable suggestions in discussing this manuscript.

References

1. Song KN, Kim SS, Lee SH, Lee SB (2009) Laser welding unit for intersection line welding of spacer grid inner straps and its application. J Laser Micro Nanoeng 4:11–17
2. Song KN, Kim SS (2007) Determination of the optimum welding parameters for a laser welded spacer grid assembly for PWRs. J Laser Micro Nanoeng 2:95–99
3. Song KN, Lee SB, Lee SH (2007) Performance evaluation of new spacer grid shapes for PWRs. Nucl Eng Technol 39:737–746
4. Song KN, Lee SB, Lee SH, Shin MK, Lee JJ, Park GJ (2010) New spacer grid to enhance mechanical/structural performance. J Nucl Sci Technol 47:295–303
5. Kang HS, Song KN, Kim HK, Yoon KN, Jung YH (2001) Verification test and model updating for a nuclear fuel rod with its supporting structure. J Korean Nucl Soc 33:73–82
6. Raynaud PA, Koss DA, Motta AT (2012) Crack growth in the through-thickness direction of hydrided thin-wall Zircaloy sheet. J Nucl Mater 420:69–82
7. Une K, Ishimoto S (2009) Crystallographic measurement of the β to α phase transformation and δ-hydride precipitation in a laser-welded Zircaloy-2 tube by electron backscattering diffraction. J Nucl Mater 389:436–442
8. Kim HG, Park SY, Lee MH, Jeong YH, Kim SD (2008) Corrosion and microstructural characteristics of Zr-Nb alloys with different Nb contents. J Nucl Mater 373:429–432
9. Qin W, Nam C, Li HL, Szpunar JA (2007) Tetragonal phase stability in ZrO_2 film formed on zirconium alloys and its effects on corrosion resistance. Acta Mater 55:1695–1701
10. Krebs B, Desquines J, Busser V, Drouan D, Zanellato O (2013) Experimental characterization of Zircaloy-4 sheet deformation during combined hydriding and corrosion. J Nucl Mater 435:41–48
11. Yao MY, Shen YF, Li Q, Peng JC, Zhou BX, Zhang JL (2013) The effect of final annealing after β-quenching on the corrosion resistance of Zircaloy-4 in lithiated water with 0.04 M LiOH. J Nucl Mater 435:63–70

12. Han Q, Kim D, Kim D, Lee H, Kim N (2012) Laser pulsed welding in thin sheets of Zircaloy-4. J Mater Process Technol 212:1116–1122
13. Tzeng YF (2000) Process characterisation of pulsed Nd:YAG laser seam welding. Int J Adv Manuf Technol 16:10–18
14. Tzeng YF, Chen FC (2001) Effects of operating parameters on the static properties of pulsed laser welded zinc-coated steel. Int J Adv Manuf Technol 18:641–647
15. Lin HL, Chou CP (2008) Modeling and optimization of Nd:YAG laser micro-weld process using Taguchi method and a neural network. Int J Adv Manuf Technol 37:513–522
16. Gao XL, Zhang LJ, Liu J, Zhang JX (2014) Effects of weld cross-section profiles and microstructure on properties of pulsed Nd:YAG laser welding of Ti6Al4V sheet. Int J Adv Manuf Technol 72:895–903
17. Dawes C (1994) Laser welding: A Practical Guide. Woodhead Publisher, England, p 16
18. Yao MY, Zhou BX, Li Q, Liu WQ, Chu YL (2006) The effect of alloying modification on hydrogen uptake of zirconium-alloy welding specimens during corrosion tests. J Nucl Mater 350:195–201
19. Kearns JJ (1967) Terminal solubility and partitioning of hydrogen in the alpha phase of zirconium, Zircaloy-2 and Zircaloy-4. J Nucl Mater 22:292–303
20. Pilling NB, Bedworth RE (1923) The oxidation of metals at high temperatures. J Inst Metals 29:529–591
21. Une K, Ishimoto S (2003) Dissolution and precipitation behavior of hydrides in Zircaloy-2 and high Fe Zircaloy. J Nucl Mater 322:66–72
22. Greger GU, Munzel H, Kunz W, Schwierczinski A (1980) A Diffusion of tritium in zircaloy-2. J Nucl Mater 88:15–22
23. Perovic V (1984) Weatherly GC The nucleation of hydrides in a Zr-2.5 wt% Nb alloy. J Nucl Mater 126:160–169